

# The Planck-LFI instrument: analysis of the $1/f$ noise and implications for the scanning strategy

D. Maino<sup>1</sup>, C. Burigana<sup>2</sup>, M. Maltoni<sup>2,3,4</sup>, B. D. Wandelt<sup>5</sup>, K. M. Górski<sup>5</sup>, M. Malaspina<sup>2</sup>, M. Bersanelli<sup>6</sup>, N. Mandolesi<sup>2</sup>, A. J. Banday<sup>7</sup>, and E. Hivon<sup>8</sup>

<sup>1</sup> SISSA, International School for Advanced Studies, Via Beirut 2-4, I-34014 Trieste, Italy

<sup>2</sup> Istituto TeSRE, Consiglio Nazionale delle Ricerche, Via Gobetti 101, I-40129 Bologna, Italy

<sup>3</sup> Dipartimento di Fisica, Università di Ferrara, Via Paradiso 12, I-44100 Ferrara, Italy

<sup>4</sup> INFN, Sezione di Ferrara, Via Paradiso 12, I-44100 Ferrara, Italy

<sup>5</sup> TAC, Theoretical Astrophysics Center, Juliane Maries Vej 30, DK-2100 Copenhagen, Denmark

<sup>6</sup> IFC, Consiglio Nazionale delle Ricerche, Via Bassini 15, I-20133 Milano, Italy

<sup>7</sup> MPA, Max Planck Inst. für Astrophysik, Karl-Schwarzschild Str. 1, D-85740, Garching, Germany

<sup>8</sup> CalTech, California Institute of Technology, 1200 East California Boulevard, CA-91125 Pasadena, USA

April 23, 2017

**Abstract.** We study the impact of  $1/f$  noise on the PLANCK Low Frequency Instrument (LFI) observations (Mandolesi et al. 1998) and describe a simple method for removing striping effects from the maps for a number of different scanning strategies. A configuration with an angle between telescope optical axis and spin-axis just less than  $90^\circ$  (namely  $\simeq 85^\circ$ ) shows good destriping efficiency for all receivers in the focal plane, with residual noise degradation  $< 1 - 2\%$ . In this configuration, the full sky coverage can be achieved for each channel separately with a  $5^\circ$  spin-axis precession to maintain a constant solar aspect angle.

**Key words:** *Methods: data analysis – Cosmology: cosmic microwave background – space vehicles*

## 1. Introduction

The great success of COBE-DMR results (Smoot et al. 1992, Bennet et al. 1996a, Górski et al. 1996) had a considerable impact on the scientific community being the first detection of CMB (Cosmic Microwave Background) anisotropy and supporting the gravitational instability scenario for structure formation. Detailed predictions for the CMB angular power spectrum in different cosmological models and the proper signature of different cosmological parameters (e.g. Zaldarriaga & Seljak 1997) are now quite well established. A significant number of new experiments, both ground-based

and balloon-borne, with sensitivity and angular resolution better than COBE (e.g. Lasenby et al. 1998 and De Bernardis & Masi 1998) are going to be designed and constructed and will deliver good quality data sets in the next few years.

It is also clear (Danese et al. 1996) that only a space mission free from unwanted contamination from ground and Earth atmosphere and with a nearly full-sky coverage can fully exploit the gold mine of cosmological information imprinted in the CMB anisotropy. The two space missions MAP (Microwave Anisotropy Probe) (see Bennet et al. 1996b) by NASA and PLANCK (Mandolesi et al. 1998, Puget et al. 1998) by ESA are planned for the next decade, the first to be launched in the year 2001 and the second in 2007. These planned observations, with their wealth of cosmological information, will play a determinant role to fully understand the properties and the evolution of the universe. In particular, PLANCK is a third-generation CMB space missions designed to achieve unprecedented sensitivity and angular resolution over the entire sky. The extremely wide frequency range ( $\simeq 30 \div 900$  GHz) explored by the combination of two focal plane arrays, the Low Frequency Instrument (LFI) and the High Frequency Instrument (HFI), will allow to efficiently separate the frequency independent primary cosmological information from astrophysical signatures (e.g. De Zotti et al. 1999) by taking advantage from their proper frequency dependencies.

As for any CMB experiment, great attention has to be devoted by the two mission teams to all the possible systematic effects. In the context of the PLANCK mission we have carried out a detailed study of one of these

effects: the so-called  $1/f$ , or low-frequency, noise which is particularly relevant for the LFI radiometers, leading to stripes in the final maps which increase the overall noise level and may alter the statistical analysis of the anisotropy distribution. Recent analytical work by Seiffert et al. (1997) has shown the dependency of the  $1/f$  noise upon the radiometer characteristics such as the bandwidth, the noise temperature, payload environment temperature and other quantities properly related to PLANCK-LFI radiometers. They can be combined to define a representative parameter, the “knee-frequency”  $f_k$ , which has to be kept as low as possible compared with the spinning frequency  $f_s$  of the spacecraft. Janssen et al. (1996) have indeed demonstrated that for  $f_k \gtrsim f_s$  a degradation in final sensitivity will result.

In Sect. 2 we briefly summarize the source of the  $1/f$  noise and the dependency of the knee-frequency upon the radiometer properties. In Sect. 3 we outline the framework of our simulations, evaluate the possible impact of  $1/f$  noise and present the technique for removing the  $1/f$  noise in the context of PLANCK-LFI. The main results both for un-reduced and reduced  $1/f$  noise are presented in Sect. 4. Our main conclusions and implications for the scanning strategy are discussed in Sect. 5.

## 2. Source of $1/f$ noise

The presence of unwanted systematic effects is one of the main difficulties in CMB anisotropy experiments. The so-called  $1/f$  noise, typically generated by HEMT (High Electron Mobility Transistor) amplifier gain instabilities, is of particular interest for the PLANCK-LFI since, if not properly corrected, it may lead to stripes in the final maps due to the satellite scanning strategy. Therefore it is of great importance to reduce the impact of such effect both by hardware and software techniques. The LFI receiver concept is driven by the need to reduce instability effects. Bersanelli et al. (1995) described the design of LFI radiometers (Fig. 1) which are modified Blum correlation receivers (Blum 1959, Colvin 1961) known also as pseudo-correlation or continuous comparison receivers. The details of the radiometer will not be described here. The main feature to note is that the receivers have two inputs: one from one of the two polarization directions of a feed-horn and one from a reference load. The signal is sent by an hybrid coupler in the two “legs” of the receiver where it is amplified and phase shifted. The signal after a second hybrid, is amplified again and detected. The output signal is proportional to the signal difference at the two inputs. This is achieved by differencing successive measurements at the detector which, for the receiver design, come from the horn and from the load respectively. The ideal situation with respect to the sensitivity to systematic effects is when the output is nulled. It is there-

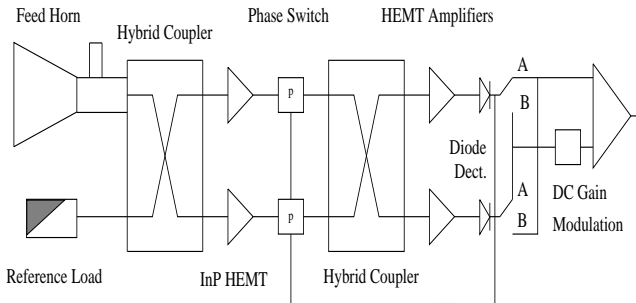


**Fig. 1.** Schematic representation of the LFI radiometers.

fore important that the temperatures of the reference load be as close as possible to the  $\approx 3$  K temperature of the sky signal. Furthermore, a nearly-null output is obtained by adjusting properly the DC gain ratio  $r$  after the diodes at the value  $r = (T_x + T_n)/(T_y + T_n)$ , where  $T_y$  is the temperature from the reference load input.

Seiffert et al. (1997) have reported an accurate analysis of the source of  $1/f$  noise in the final output of this receiver design. The ideal white noise sensitivity for this kind of radiometer is given by:

$$\Delta T_{\text{wn}} = \frac{\sqrt{2}(T_n + T_x)}{\sqrt{B\tau}}, \quad (1)$$

where  $B$  is the bandwidth (for LFI 20% of the central frequency),  $\tau$  is the integration time,  $T_x$  is the signal at horn input and  $T_n$  is the noise temperature of the amplifier. The main source of  $1/f$  noise resulted be gain fluctuations in the HEMT amplifiers which have a typical  $1/f$  spectrum. These fluctuations translate into fluctuations of the noise temperature  $T_n$  with the same spectral shape. Noise temperature fluctuations  $\Delta T_n$  can mimic a change in the radiometer output

$$\Delta T_{\text{equiv}} = \sqrt{2}\Delta T_n \left[ \frac{1-r}{2} \right] = \sqrt{2} \left[ \frac{A \times T_n}{\sqrt{f}} \right] \left[ \frac{1-r}{2} \right], \quad (2)$$

where  $A$  is the square root of the spectral amplitude of noise temperature fluctuations. Following Seiffert et al. (1997), we define the “knee-frequency” when  $\Delta T_{\text{equiv}} = \Delta T_{\text{wn}}$ . This leads to the expression

$$f_k = \frac{A^2 B}{8} (1-r)^2 \left( \frac{T_n}{T_n + T_x} \right)^2. \quad (3)$$

Typical values are  $A \sim 1.8 \times 10^{-5}$  for 30 and 44 GHz radiometers and  $A \sim 2.5 \times 10^{-5}$  for 70 and 100 GHz. Fig. 2 reports an example of simulated output for a pure white noise and a white noise plus  $1/f$  noise signal: their difference is much more clear in Fourier space where the  $1/f$  noise spectrum shows up at low frequencies. For the

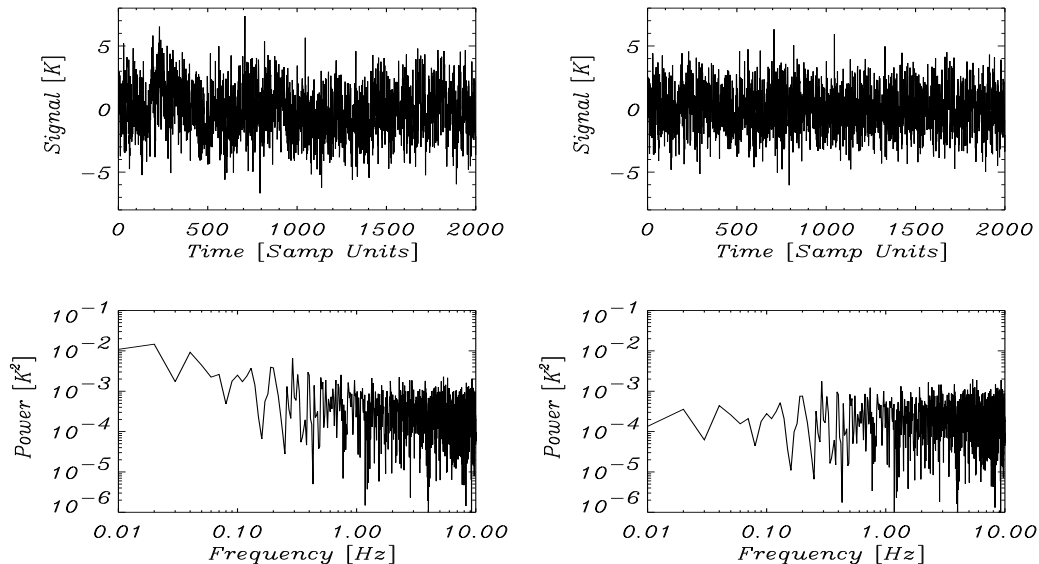


**Fig. 2.** Comparison between a pure white noise (right) and white+ $1/f$  noise (left) in time domain (upper panels) and and Fourier space (bottom panels). Their difference is more clear in Fourier space with a flat spectrum for the white noise and the typical  $1/f$  noise spectrum for the low-frequency noise. We used a  $f_k = 0.8$  Hz for this illustrative case

30 GHz channel, with  $T_n = 9$  K,  $T_x = 3$  K,  $B=6$  GHz,  $T_y = 20$  K Eq.(3) gives a  $f_k \sim 0.046$  Hz. For a 4 K reference load, which is now the adopted baseline, the knee-frequency reduces to  $\approx 1$  mHz. For the 100 GHz channel  $f_k$  is higher (0.11 Hz) for a 20 K reference load and is reduced to less than 1 mHz for the 4 K load.

### 3. Scan circles, sky maps and destripping

As reported in Mandolesi et al. (1998), the selected orbit for PLANCK satellite will be a Lissajous orbit around the L2 Lagrangian point of the Sun-Earth system. The spacecraft spins at 1 r.p.m. and the spin axis is kept on the Ecliptic plane at constant solar angle by re-pointing of  $2.5'$  every hour. The field of view of the two instruments is between  $\alpha \approx 80^\circ - 90^\circ$  from the spin-axis direction. Hence PLANCK will trace large circles in the sky: these circles cross each other in regions close to the Ecliptic poles. The shape and width of these regions depend upon the angle  $\alpha$ , the scanning strategy and beam location in the focal plane. The value of the angle  $\alpha$  has not yet been fully defined, as well as the scanning strategy, which may or may not include a periodic motion of the spin-axis away from the Ecliptic plane. These options depend on a trade-off between different systematic effects (striping, thermal effects, straylight), which has to be carefully addressed.

Here we made an attempt in this direction taking into consideration the  $1/f$  noise alone as if all the other systematics were negligible. This is of course an idealised situation but gives us an estimate of the impact of this

effect that therefore should be regarded as a lower limit. Nonetheless this result may help for a better design of the instrument. Future work will consider a more complete situation when a detailed thermal transient analysis will be available for the Planck spacecraft.

#### 3.1. The “flight-simulator”

Burigana et al. (1997, 1998) has described in detail the code we have implemented for the PLANCK scanning strategy and we refer the reader to these papers. The relevant geometrical inputs are the beam location in the focal plane and the angle  $\alpha$  between the spin and pointing axis.

For each beam position on the focal plane our code outputs the complete data stream. We consider here a reduced version of the actual baseline for the scanning strategy (actual parameters in parentheses): spin-axis shift of  $5'$  every 2 hours (instead of  $2.5'$  every hour) and three samplings per FWHM of  $30'$  at 30 GHz (instead of 12 samplings every  $30'$ , i.e. 4 samplings every  $10'$ , the FWHM at 100 GHz; see Mandolesi et al. 1998). These modifications allow us to explore a large region of the parameter space, beam position,  $f_k$ , scanning strategy and pointing angle  $\alpha$ , in reasonable time. Furthermore we do not consider the single minute data stream but we take the average over the 120 circles forming a given 2-hours set. In what follows we run simulations for the 30 GHz channel.

Wright (1996) has shown that possible data filtering on a given scan circle may help in reducing the impact

of  $1/f$  noise. This is useful for values of  $f_k$  typical for “total power” receivers which are much higher than our 0.05 Hz and we chose not to include this technique here.

It is clear from Eqs.(1) and (3) that both the sensitivity and the “knee-frequency” depend on the actual temperature in the sky  $T_x$  seen by the horn. Our synthetic model for microwave sky emission includes a standard CDM prediction for CMB fluctuations plus a model of galactic emission. This model has the spatial template from the dust emission (Schlegel et al. 1998) but has been normalized to include contribution from synchrotron, free-free and dust according to *COBE*-DMR results (Kogut et al. 1996). The major foreground contamination at 30 GHz comes from synchrotron and free-free. We then choose to overestimate the overall synchrotron fluctuations by a factor of  $\approx 10$ . This is the worst case scenario with respect to destriping efficiency (see Sect. 3.3 and 3.4).

Of course the impact of the sky temperature is small, since  $T_x$  is a small fraction of the noise temperature  $T_n$ : this is in fact  $\sim 10$  K while  $T_x \approx 3$  K at 30 GHz and the maximum galactic contamination adopted here is about 44 mK. In this evaluation of  $T_x$  we include also a typical environment temperature of about 1 K.

We do not perform a convolution with a real beam pattern and sky signal since the real beam pattern will be in general not perfectly symmetric, not perfectly gaussian and with sidelobe contributions which will introduce other kinds of contamination. Since we want to estimate here only the impact of  $1/f$  noise we convolve our input map with a gaussian beam with the nominal FWHM (33') of the 30 GHz PLANCK-LFI channel we consider.

### 3.2. Generation of instrumental noise

We have the possibility to generate different kinds of noise spectra. We work in Fourier space and generate the real and imaginary part of Fourier coefficients of our noise signal. The noise spectrum has the usual form:

$$S_{noise}(f) = a \left[ 1 + \left( \frac{f_k}{f} \right)^\beta \right], \quad (4)$$

where  $a$  is a normalization factor and  $\beta$  takes typical values from 1 to 2.5 depending on the source of noise (gain drift of thermal effects):  $\beta = 1$  is the  $1/f$  noise case. In general it is a good approximation to take  $S_{noise}(f)$  vanishing for  $f < f_{min}$  and  $f > f_{max}$ . Delabrouille (1998) proposed  $f_{min} \sim 1/T_{mission}$  and  $f_{max} \sim 1/2T_{samplings}$ .

After generating a realisation of the real and imaginary part of the Fourier coefficients with spectrum defined in Eq.(4), we FFT (Fast Fourier Transform; Cooley & Tukey 1965; Heideman et al. 1984) them and obtain a real noise stream which has to be normalized to the white noise level defined in Eq.(1). We use a typical value of  $f_k = 0.05$  Hz for the knee-frequency at 30 GHz assuming

a 20 K load temperature (see Sect. 2). We chose to generate noise streams of about  $2 \times 10^6$  data points, corresponding to 8 spin axis positions or 16 hours: this seems a reasonable compromise among our present knowledge of real hardware behaviour and the required computational time with respect noise stream length. The actual time for a generation of a noise stream 16 hours long and one year of mission even in our reduced scanning strategy will require about 10 hours on a Silicon Graphics machine with 2 Gb of RAM and clock speed of 225 MHz. We also verified that the most time consuming operation in our code is just the FFT  $1/f$  noise generation.

The possibility to generate the noise streams with a completely arbitrary spectrum in real space (e.g. Beccaria et al. 1996 and Cuoco & Curci 1997 and references therein), without the use of FFT, seems very promising for considerably reducing the computational time (Wandelt et al. 1999, Wandelt & Górski 1999).

### 3.3. From data stream to sky maps

The final output of our “flight-simulator” are 4 matrices with a number of rows equal to the considered spin-axis positions  $n_s$  (for one year of mission  $\sim 4320$  in our reduced baseline as in Sect.3.1) and a number of columns equal to the number of integrations, weakly dependent on  $\alpha$ , along one scan circle (here  $n_p \sim 2160$ ). The input and output maps are in HEALPix pixelisation scheme (Górski et al. 1998, <http://www.tac.dk/~healpix>); we use an input map with a resolution of about 3.5' corresponding to 12 million equal area pixels on the full sky.

For each circle, the code outputs are the pixel number  $\mathbf{N}$  at the specified resolutions, the temperature plus total noise contribution  $\mathbf{T}$  (white plus  $1/f$  noise), the temperature with only white noise  $\mathbf{W}$  and the pure signal as observed in absence of instrumental noise  $\mathbf{G}$ . The  $\mathbf{W}$  and  $\mathbf{G}$  will be used for studying the degradation of  $1/f$  noise with respect to the ideal pure white noise case and the impact of scanning strategy geometry on observed pixel temperatures.

We can arbitrarily choose the temperature output data stream resolution from 3.5' to higher values (smaller resolution) which set also the output temperature map resolution. Regarding the data stream for the pixel number outputs we can also use higher resolutions, allowing to test the impact of using more or less stringent crossing conditions in the destriping algorithm (see the following section).

From these data streams it is quite simple to obtain observed simulated maps: we make use of  $\mathbf{N}$  and  $\mathbf{T}$  to coadd the temperatures of those pixels observed several times during the mission. In the same way we build maps with only white noise contribution, without receiver noise, as well as a sensitivity map knowing how many times a single pixel is observed.

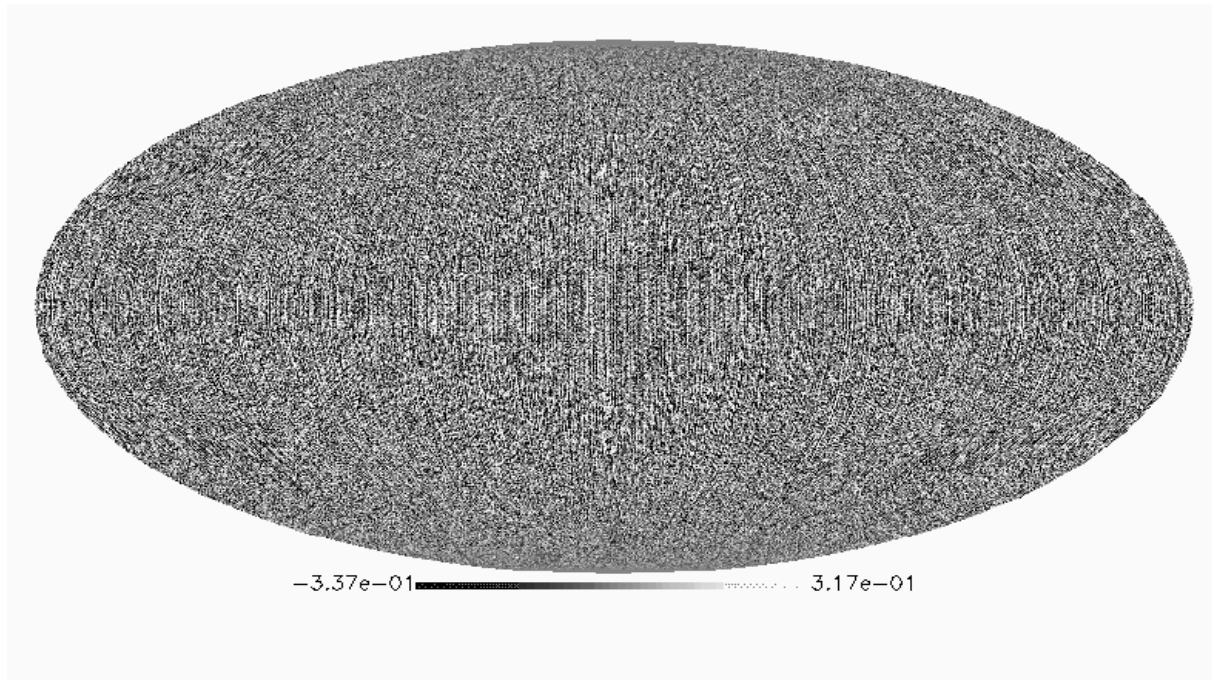


**Fig. 3.** Pure noise (white and  $1/f$  noise together) map before destriping: stripes are clearly present. The adopted  $f_k$  is 0.05 Hz and units are in mK. See the text for simulation input parameters.

In Fig. 3 we show a pure noise (white plus  $1/f$ ) map in Ecliptic coordinates after signal subtraction ( $\mathbf{T} - \mathbf{G}$ ): stripes are clearly present.

the result will be matrices with  $n_s \times n_l$  rows and  $n_p/n_l$  columns.

### 3.4. Destriping techniques

We developed a simple technique which is able to eliminate gain drifts due to  $1/f$  noise. This is derived from the COBRAS/SAMBA Phase A study proposal (Bersanelli et al. 1996) and from a re-analysis of Delabrouille (1998). As reported by Delabrouille (1998) the effect of  $1/f$  noise can be seen as one or more additive levels, different for each scan circle. We worked with averaged (over 2 hours period) scan circles and hence we nearly removed drifts within each circle: what is left is related to the “mean”  $1/f$  noise level for this observation period. In fact averaging scan circles into a single ring corresponds to a low-pass filtering operation. As long as  $f_k$  is not far larger than the spin frequency, this ensures that only the very lowest frequency components of the  $1/f$  noise survive. Therefore it is a good approximation to model the averaged  $1/f$  noise as a constant offset  $A_i$  for each ring for the set of parameters we are using.

We want to obtain the baselines for all the circles and re-adjust the signals correspondingly. Delabrouille (1998) claimed the possibility that working with multiple baseline per circle ( $n_l =$  number of baseline levels) may result in a better destriping. In our code this is equivalent to dividing the rows of each output matrices in  $n_l$  parts:

In order to estimate the different  $A_i$  we have to find common pixels observed by different scan circles and the pixel size in the matrix  $\mathbf{N}$  is a key parameter. Increasing the resolution used in  $\mathbf{N}$  reduces the number of crossings possibly yielding to lower destriping efficiency, while adopting resolutions lower than the resolution of the input map and of the matrix  $\mathbf{T}$  introduces extra noise, related to variations of real sky temperature within the scale corresponding to the lower resolution adopted in  $\mathbf{N}$ , which is not taken into account in the estimate of receiver noise and may introduce artifacts in the destriping code. The adopted pessimistic galactic emission model, which by construction has gradients larger than those inferred by current data, emphasizes this effect and our simulations are then conservative in this respect. In the following  $N_{il}$ ,  $T_{il}$  and  $E_{il}$  will denote the pixel number, the temperature and the white noise level for the pixel in the  $i^{\text{th}}$  row and  $l^{\text{th}}$  column. Let us denote a generic pair of different observations of the same pixel with an index  $\pi$  which will range between 1 and  $n_c$ , the total number of pairs found. In this notation  $\pi$  is related to two elements of  $\mathbf{N}$ :  $\pi \rightarrow (il, jm)$  where  $i$  and  $j$  identify different scan circles and  $l$  and  $m$  the respective position in each of the two circles.

We want to minimize the quantity:

$$S = \sum_{\text{all pairs}} \left[ \frac{[(A_i - A_j) - (T_{il} - T_{jm})]^2}{E_{il}^2 + E_{jm}^2} \right] \\ = \sum_{\pi=1}^{n_c} \left[ \frac{[(A_i - A_j) - (T_{il} - T_{jm})]^2}{E_{il}^2 + E_{jm}^2} \right]_{\pi} \quad (5)$$

with respect to the unknown levels  $A_i$ . The sub-index  $\pi$  indicates that each set of  $(il, jm)$  is used in that summation. It is clear that  $S$  is quadratic in all the unknown  $A_i$  and that only differences between  $A_i$  enter into Eq.(5). Therefore the solution is determined up to an arbitrary additive constant (with no physical meaning for anisotropy measurements). We choose then to remove this indetermination by requiring that  $\sum_{h=1}^{n_s} A_h = 0$ . This is equivalent to replace Eq.(5) with  $S' = S + \left( \sum_{h=1}^{n+s} A_h \right)^2$ . After some algebra we finally get:

$$\frac{1}{2} \frac{\partial S'}{\partial A_k} = \sum_{\pi=1}^{n_c} \left[ \frac{[(A_i - A_j) - (T_{il} - T_{jm})] \cdot [\delta_{ik} - \delta_{jk}]}{E_{il}^2 - E_{jm}^2} \right]_{\pi} \\ + \sum_{h=1}^{n_s} A_h = 0 \quad (6)$$

for all the  $k = 1, \dots, n_s$  (here  $\delta$  is the usual Kronecker symbol). This translates into a set of  $n_s$  linear equation

$$\sum_{h=1}^{n_s} C_{kh} A_h = B_k, \quad k = 1, \dots, n_s \quad (7)$$

which can be easily solved. Furthermore we note that by construction the matrix  $\mathbf{C}$  of  $C_{kh}$  coefficients is symmetric, positive defined and non singular. The first property permits to hold in memory only one half of the matrix  $\mathbf{C}$  (e.g. the upper-right part), the second allows us to solve the linear system without having to exchange rows or columns (Strang 1976), so preserving the symmetry. The non-singularity of  $\mathbf{C}$  is true provided that there are enough intersections between different circles and hence is related to the resolution at which we look for common pixels between different scan circles, to the scanning strategy and beam location. A detailed discussion of numerical algorithm for solving this system with significant saving of required RAM is presented in Burigana et al. (1997).

It is interesting to note that the applicability of this destriping technique does not depend upon any a-priori assumption about the real value of  $f_k$  or the real noise spectral shape since it can work also for different values of the exponent  $\beta$  in Eq.(4), although its efficiency could be in principle partially optimized in relation to the properties of the noise and of the sky gradients.

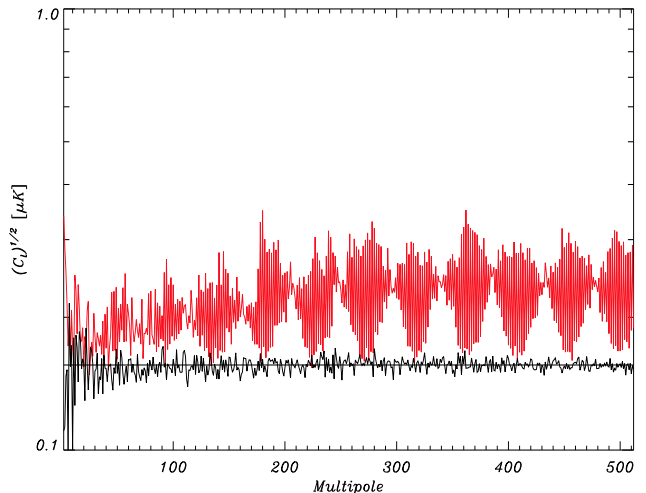


**Fig. 4.** Noise power spectra at 30GHz before destriping. Simulations parameters are:  $\alpha = 90^\circ$ ,  $(\theta_B, \phi_B) = (2.8^\circ, 45^\circ)$ ,  $f_k = 0.05$  Hz and spin-axis always on the Ecliptic plane. Theoretical white noise level is also reported for comparison. The excess of noise is about 40% over the white noise level.

#### 4. Simulations results and scanning strategy

We first consider an angle  $\alpha = 90^\circ$  between telescope and spin axes and a beam location with  $(\theta_B, \phi_B) = (2.8^\circ, 45^\circ)$ . Here  $\theta_B$  is the angle from the optical axis: this is a typical value for the 100 GHz (with a  $\simeq 1.5$  m aperture off-axis Gregorian telescope) horns while the 30 GHz beams are placed at larger  $\theta_B$  values. This assumption is therefore conservative with respect to the destriping efficiency, since in this case the region of crossings between scan circles is smaller and closer to Ecliptic poles. The angle  $\phi_B$  is the beam center displacement from the axis given by the intersection between the sky field of view plane and the plane containing the telescope and spin axes (see Burigana et al. 1998). Our choice of  $\phi_B = 45^\circ$  is intermediate between  $0^\circ$  (or  $180^\circ$ ) and  $90^\circ$  which are equivalent for the destriping respectively to an on-axis beam (with crossings only at Ecliptic poles for  $\alpha = 90^\circ$ ) and a beam which spreads crossings over the wider possible region. The adopted beam location is therefore a non-degenerate case although non optimal.

The knee frequency  $f_k = 0.05$  Hz and the microwave sky emission is modeled as in Sect.3.1.

We evaluated the impact of  $1/f$  noise both in terms of added *rms* noise and of angular power spectrum. The output of our simulations is expressed in antenna temperature and has to be converted into thermodynamic temperature for the comparison with CMB power spectrum, as usually predicted in theoretical models. At 30 GHz the conversion factor is very close to unity ( $rms_{th} \simeq rms_A$ , where  $rms_A$  is the *rms* in antenna temperature).

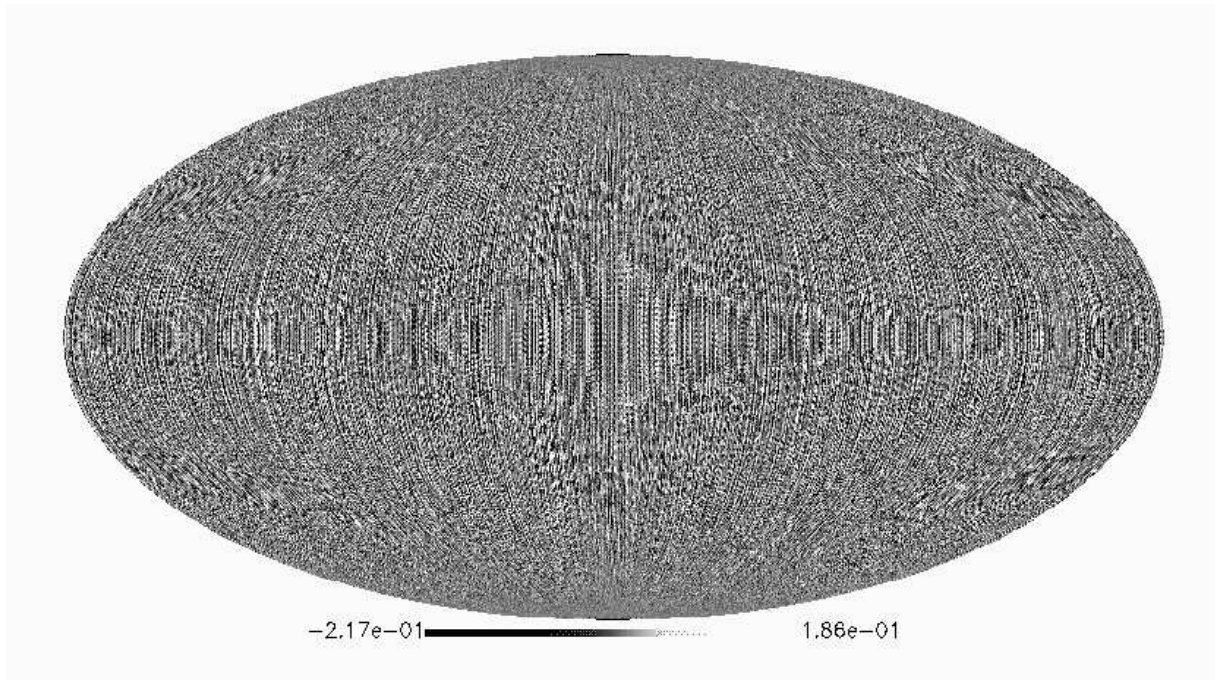


**Fig. 5.** Baselines recovered from destripping algorithm for the case reported in Fig 3.

The white noise power spectrum can be derived analytically knowing the total number of pixels in the sky and pixel sensitivity :

$$C_{\ell,wn} = \frac{4\pi}{N_{\text{pix}}^2} \sum_{i=1}^{N_{\text{pix}}} \sigma_i^2 = \frac{4\pi}{N_{\text{pix}}} \langle \sigma^2 \rangle. \quad (8)$$

#### 4.1. Morphology of the $C_\ell$ artefacts due to 1/f noise

We now give a short theoretical argument for the expected morphology of the  $C_\ell$  power spectra of the simulated striping pattern. For scanning without wobbling or precession, two angular scales fully determine the structure of the striping pattern on the sky. One is the half opening angle  $\lambda_1 = 90^\circ$  of the ecliptic equator which the spin axis traces on the sky as PLANCK completes a full orbit about the sun. This makes the noise pattern symmetric under parity, on average. It follows that the correlation function for the noise pattern is symmetric about  $90^\circ$ , with a strong peak at  $180^\circ$  and for the 1/f component  $C_\ell = 0$  for all odd  $\ell$ .

The other scale is the half opening angle of the scanning rings  $\lambda_2 \simeq \alpha - \theta_B \sin(\phi_B)$ ,  $\theta_B \ll \pi/2$ . This leads to peaks in the correlation function at  $2\lambda_2$  and by symmetry at  $180^\circ - 2\lambda_2$ .

The combination of these two nearby scales leads to beats in the  $C_\ell$ , which are visually apparent as the “blob” in Figs. 4,8,10,12 and 14. Treating this effect in the same way as the appearance of fringes in an interference pattern we can calculate the width in  $\ell$  of each blob

as  $\Delta\ell = 90/(\lambda_2 - \lambda_1)$ . This is in quantitative agreement with our numerically computed spectra. It also explains the absence of beats in Figure 10, where  $\lambda_2 = \lambda_1 = 90^\circ$  and the power spectrum can be understood as a single blob with infinite  $\Delta\ell$ .

For scanning strategies with some kind of “wobble”, ie. where the spin axis does not trace out the ecliptic equator on the sky, the correlation function will still be approximately symmetric if the amplitude of the wobble is small compared to  $90^\circ$  and the above statements remain approximately true. However, the fact that the symmetry is weakly broken can be seen in Figure 8, where the interference effect is slightly washed out and the beats do not reach all the way down to the white noise level.

The offset of the blobs compared to the white noise level is given by the *rms* excess power due to the 1/f noise component. At first sight it may be surprising that other than this normalisation, the shape of the excess power power spectrum  $C_\ell$  of the striping pattern is independent of the spectral content of the noise, as parametrised by the knee frequency. This is due to the filtering effect of co-adding scan circles into rings discussed above. In the regime which our simulations probe, the structure which remains on each ring is well described by a constant offset plus white noise. Hence, as long as sufficiently many scan circles are co-added, changing the knee frequency simply scales the relative contribution of 1/f and white noise to the noise pattern  $C_\ell$ .

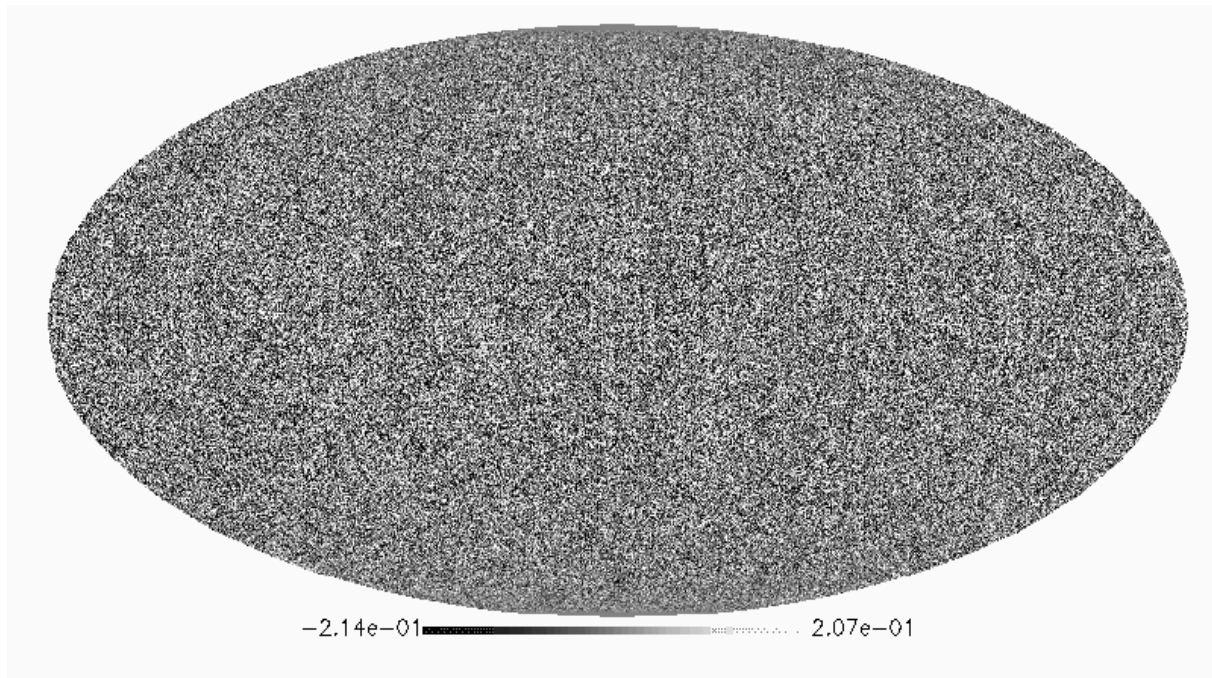


**Fig. 6.** Noise map after destriping for the same case illustrated in Fig. 3: stripes are no more visible.

#### 4.2. Simulation results

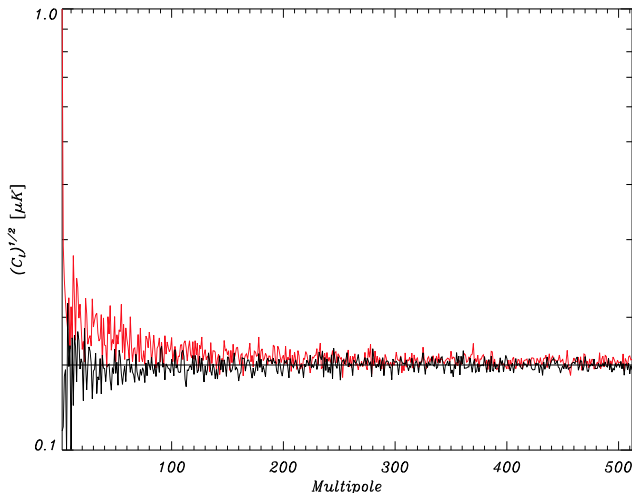
In Fig. 4 we show the square root of the power spectrum (which is roughly proportional to  $rms$  contribution of temperature per  $\ell$ -bin) before applying the destriping technique: the solid line is the white noise level as derived from Eq.(8) and the superimposed spectrum is derived from a simulation with only white noise included. The agreement is very good which confirms the accuracy of our simulator and map-making algorithm. The gray line is the global noise spectrum (white and  $1/f$  noise together). The spectrum is clearly non-white: blobs are present. The excess of noise in terms of both  $rms_{th}$  and  $\sqrt{C_\ell}$  is about 40% of white noise level.

Fig. 6 shows the noise map after applying our destriping code: stripes are no more evident and Fig. 5 shows the recovered baselines by destriping algorithm. This situation can be quantified by computing the noise power spectrum of the destripped map, as shown in Fig. 7. Now the spectrum is considerably flatter and no more blobs are present, with an overall noise excess of 1-2% over the white noise level. This confirms the efficiency of the destriping algorithm, under the above mentioned simplifying assumptions. On the other hand it is clear from Fig. 7 that at large scales, corresponding to  $\ell \lesssim 100$ , a non-negligible residual contribution is present in the noise spectrum. A lower knee frequency (achievable with the reference loads at 4K) is necessary to further reduce the effect. We also investigated if different scanning strategies may help in destriping efficiency.

Possible periodic motion of the spin-axis away from the Ecliptic plane have the effect of broadening the region of crossings between different circles. This goes in the direction of removing possible degeneracies in the destriping system. We implemented both sinusoidal oscillations and precessions: the first does not preserve the spacecraft solar illumination and this is likely to induce thermal effects and drifts in the data.

The second is then preferable, since it keeps the solar angle constant as the satellite moves the spin-axis. For both the motions we performed 10 complete oscillations per year of mission with  $10^\circ$  amplitude. The results before and after destriping are nearly the same for the two cases and Fig. 8 and Fig. 9 report noise power spectra for the precession motion: before destriping blobs are still present and disappear after destriping. The excess of noise is  $\sim 40\%$  and 1-2% before and after destriping respectively.

We consider also a case of an on-axis beam  $(\theta_B, \phi_B) = (0^\circ, 0^\circ)$  with  $\alpha = 90^\circ$ . This situation is representative of horns which, in the focal plane arrangement, are placed close to the scanning direction: from the destriping point of view these horns are indeed equivalent to on-axis horns and intersections between different scan circles are nearly only at Ecliptic poles. This represents a degenerate situation with respect to destriping efficiency. Fig. 10 and Fig. 11 show noise power spectra for this on-axis case before and after destriping respectively: the geometry of the simulation is changed and the same for blob shape which is not well defined. Here the level of



**Fig. 7.** Noise power spectra at 30GHz after destriping. Simulation parameters are the same of Fig. 4. Now the added noise is only 1-2% of the white noise level. White noise spectra are also reported for comparison.

added noise is  $\sim 42\%$ . After destriping we are left with an excess of noise of the order of 5% of the white noise and the noise spectrum is considerable less flat than before. Such excess noise and a non-flat spectrum around  $\ell \sim 100 - 200$  (where the first CMB Doppler peak is expected) after destriping is clearly not acceptable for the feeds aligned with the scan direction. Moving the spin axis is a way to remove this degeneracy, as well as to complete the sky coverage for all channels. Keeping fixed the beam position we move the angle  $\alpha$  from  $90^\circ$  to  $85^\circ$ : this of course leaves small regions around Ecliptic poles which are not observed but has the advantage to enlarge the scan circle crossing region. Fig. 12 and Fig. 13 show noise power spectra before and after destriping respectively for this  $85^\circ$ , on-axis case: now blobs are clearly visible with dimensions in  $\ell$ -space different from Fig. 4 due to different geometrical configuration. These blobs are completely removed after destriping leaving a level of added noise after destriping of only  $\lesssim 2\%$  over the white noise. This is essentially what we obtained for the off-axis configuration. All the simulations considered so far were performed with a  $f_k = 0.05$  Hz which is derived from Eq.(3) assuming a  $T_y = 20$  K of reference load. To decrease the residual effect, a 4 K reference load is being designed, exploiting the 4 K stage of the HFI. In this configuration it is expected that the resulting knee frequency would be less than 10 mHz. We have run a simulation with  $f_k = 0.01$  Hz with the usual off-axis configuration with  $\alpha = 90^\circ$ . As for the other cases we report noise power spectra before and after destriping in Fig. 14 and Fig. 15. It is interesting to note that now the

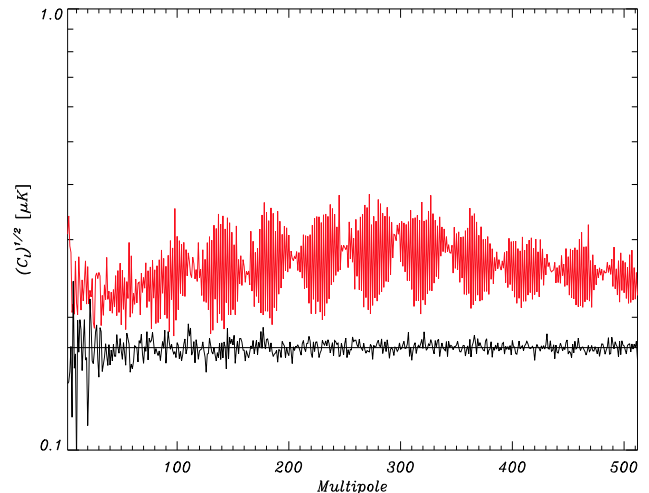


**Fig. 8.** Noise power spectra at 30GHz Before destriping. Simulation parameters are the same of Fig. 4 except for the scanning strategy which includes here precession (see the text). The added noise is  $\sim 40\%$  of the white noise level. White noise spectra are also reported for comparison.

level of added noise is 9% before destriping and reduces only to 0.5% after applying destriping algorithm.

Although a comparison among different kinds of systematic effects (Burigana et al. 1999) and studying how they combine in LFI observations is out of the aim of the present work, we have tried a first attempt in considering the sensitivity of this destriping algorithm to one of the most relevant source of contamination in Planck measurements, the beam shape asymmetry. We have considered two simulations: one with a pure circular gaussian beam and another with a highly elliptical gaussian beam with a ratio of 1.7 between major and minor axis, that exhibit rms differences of about  $5 \mu\text{K}$  in the temperatures observed in the same sky directions (Burigana et al. 1998). The impact of beam ellipticity on destriping efficiency appears to be small: it has a maximum effect which is  $\sim 3$  times smaller than the white noise level between  $100 < \ell < 200$  (Burigana et al. 1999). This preliminary result suggests that the adopted algorithm may be only weakly dependent on the contamination introduced by other kinds of systematic effects; further investigations are demanded to confirm this perspective.

## 5. Discussion and conclusion

We have reported here an extensive study of the  $1/f$  noise contamination for different scanning strategies, beam location on the focal plane as well as for different values of the knee frequency. Even in this idealised situation (all other systematics are well under control) we can gain useful information from our study.

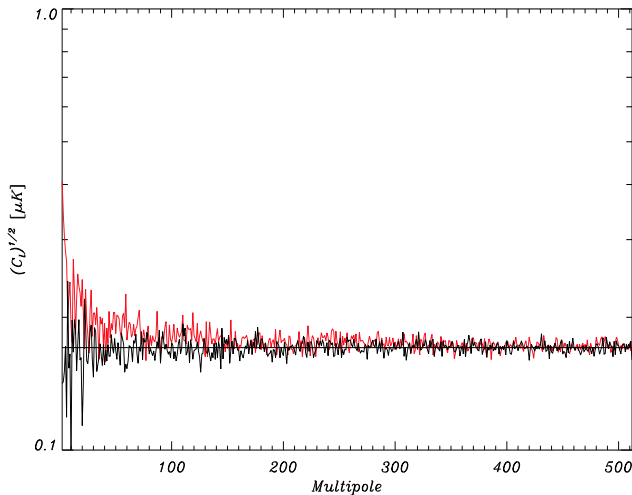


**Fig. 9.** Noise power spectra at 30GHz after destriping. Simulation parameters are the same of Fig. 8. The added noise is now only 1-2% of the white noise level. White noise spectra are also reported for comparison.

First of all from these simulations it seems that moving the spin-axis away from the ecliptic plane does not significantly help the destriping efficiency for typical LFI beam locations and, concerning the  $1/f$  noise alone as source of drifts, it would be preferable to keep the spin-axis always on the Ecliptic plane. This is clear when we compare results as those in Fig 7 and Fig. 9 which are practically identical.

Furthermore for most of the LFI beams the choice of  $\alpha = 90^\circ$  would be acceptable: the destriping left only  $\lesssim 2\%$  of excess noise with respect to the pure white noise case. On the other hand, some LFI beams are equivalent to on-axis beam which, from Fig. 11, is clearly a degenerate case. A smaller value of  $\alpha$  (namely  $85^\circ$ ) breaks this degeneracy at an acceptable level yielding the usual destriping efficiency. From these two points an indication of a possible choice of the scanning strategy and instrument configuration arises: with  $\alpha = 85^\circ$  and precession of the spin-axis (no thermal drifts) with only  $5^\circ$  amplitude (half of what we considered here) appears satisfactory for destriping performances while preserving full-sky coverage for all channels. This allows data redundancy but introduces irregularities in the integration time distribution, which may be an issue for the data analysis. Without spin axis modulations, a quite complete sky coverage and a smooth integration time distribution at each frequency can be achieved only by assembling data from different receivers, losing redundancy.

We have considered also the destriping efficiency when using more than a single baseline level  $A_i$  per scan circle: results reported in Burigana et al. (1997) indicate that for the  $1/f$  noise case no significant improvements

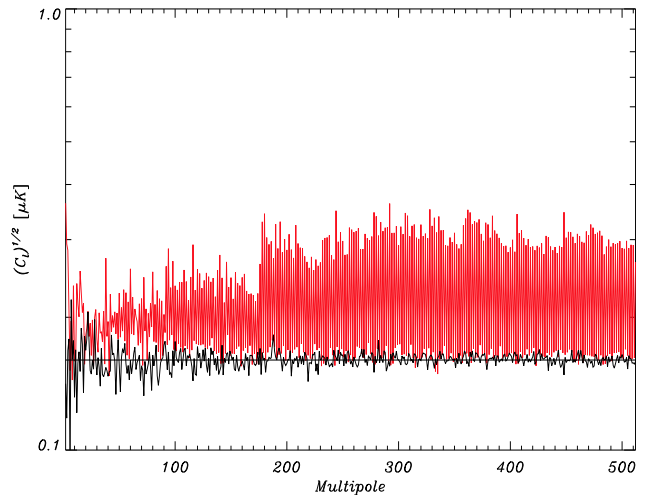


**Fig. 10.** Noise power spectra at 30GHz Before destriping. Simulation parameters are the same of Fig. 4 but the beam position is now  $(\theta_B, \phi_B) = (0^\circ, 0^\circ)$ . The added noise is  $\sim 42\%$  of the white noise level. White noise spectra are also reported for comparison.

are achieved: either the  $1/f$  noise level per circle is almost constant and equivalent to a single baseline, or the accuracy in the determination of more levels per circle decreases. The whole set of simulations seems to indicate that there is enough redundancy of observations to remove at acceptable level the contamination due to  $1/f$  noise even if we require a more strict condition of crossings between scan circles. Of course, the performance of this destriping code could be partially optimized in the future by appropriately choosing the number of levels per circle and the crossing condition according to the dominant kind of instrumental noise (the parameters  $f_k$  and  $\beta$ ), the magnitude of the gradients in the sky emission and our knowledge of other contamination sources.

For what concerns properly the  $1/f$  noise, an important indication comes from the simulation with  $f_k = 0.01$  Hz: the excess of noise before destriping reduces by a factor  $\simeq 4$  with respect to the case  $f_k = 0.05$  Hz. Reaching  $f_k = 0.01$  Hz is a goal of the LFI design, which will ensure a clean and robust observation. In addition the extra noise level after destriping decreases, at least under these ideal assumptions, by a factor  $\simeq 3$ .

There are many open issues both astrophysical and instrumental. Regarding the first, the microwave emission model we use, although pessimistic for what concerns galactic emission, can be completed with the inclusion of different foreground contributions. The emission from extragalactic point sources and in particular their variability may decrease our destriping efficiency. We have also not considered here any other source of possible systematic effects such as thermal effects and

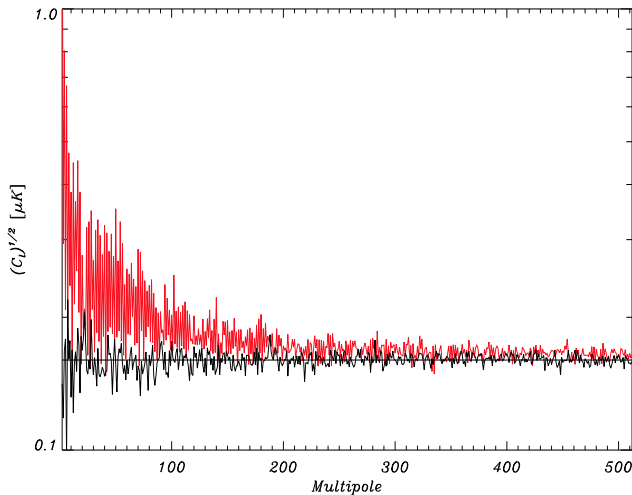


**Fig. 11.** Noise power spectra at 30GHz after destriping. Simulation parameters are the same of Fig. 10. The added noise is now larger than previous cases, being 5% of the white noise level. White noise spectra are also reported for comparison.

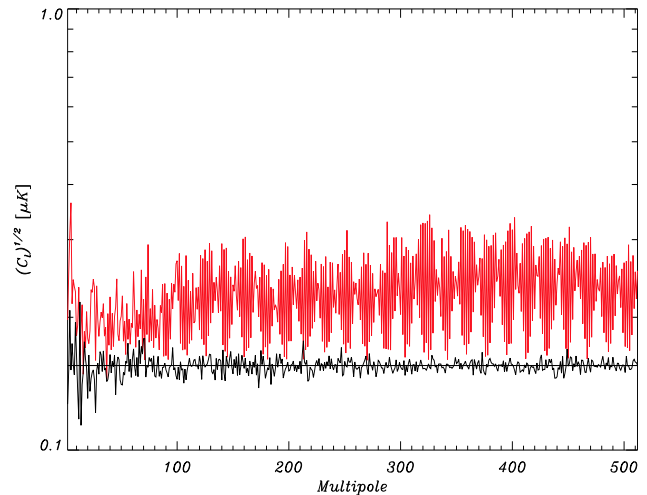


**Fig. 12.** Noise power spectra at 30GHz Before destriping. Simulation parameters are the same of Fig. 10 but the angle  $\alpha$  is now set to  $85^\circ$ . The added noise is  $\sim 42\%$  of the white noise level. White noise spectra are also reported for comparison.

stray-light contamination induced by Galaxy emission. Burigana et al. (1999) describe in detail the impact of stray-light contamination. Also these effects may in principle degrade the accuracy in removing  $1/f$  noise stripes.

As proved by the scientific experience in many years of work both in physics and in cosmology and astrophysics, efficient data analysis tools can significantly improve the quality of the information extracted from the data, provided that the systematic effects are well understood, but the first and most important step in projecting experiments is to reduce all the contaminations at the lowest possible levels. It is then of great importance to decrease as much as possible the impact of  $1/f$  noise before destriping and  $f_k = 0.01$  Hz is an important goal for instrument studies and prototypes.

*Acknowledgements.* We gratefully acknowledge stimulating and helpful discussions with L. Danese, J. Delabrouille and M. Seiffert.

## References

- Beccaria, M., et al., 1996, “Gravitational wave search: real time data analysis strategies on parallel computers”, NTS-96024.
- Bennet, C. et al., 1996a, ApJ, 464, L1.
- Bennet, C. et al., 1996b, Amer. Astro. Soc. Meet., 88.05.
- Bersanelli, M. et al., 1995, Int. Rep. TeSRE/CNR 177/1995.
- Bersanelli, M. et al., 1996, ESA, COBRAS/SAMBA Report on the Phase A Study, D/SCI(96)3.
- Blum, E.J., 1959, Annales d’Astrophysique, 22-2, 140.
- Burigana, C. et al., 1997, Int. Rep. TeSRE/CNR 198/1997.
- Burigana, C. et al., 1998, A&ASS, 130, 551.
- Burigana, C. et al., 1999, A&A, to be submitted.
- Colvin, R.S., 1961, Ph.D. Thesis, Stanford University.
- Coolet, J.W. & Tukey, J.W., 1965, “An algorithm for machine calculation of complex Fourier series”, Math. Computat., vol. 19, 297.
- Cuoco, E., & Curci, G., 1997, “Modeling a VIRGO-like noise spectrum - Note 1”, VIR-NOT-PIS-1390-095, 14/07/97.
- Danese, L. et al., 1996, Astro. Lett. Comm., 35, 257.
- De Bernardis, P. & Masi, S., 1998, Proceedings of the XXXIII<sup>rd</sup> Rencontres de Moriond, pg. 209.
- Delabrouille, J., 1998, A&ASS, 127, 555.
- De Zotti, G. et al., 1999, to appear in Proceedings of the Conference “3 K Cosmology”, Roma, Italy, 5-10 October 1998, AIP Conference Proc, astro-ph/9902103.
- Górski, K. M. et al., 1996, ApJ, 464, L11.
- Górski, K. M., Hivon, E., & Wandelt, B. D., 1998, to appear in “Proceedings of the MPA/ESO Conference on Evolution of Large-Scale Structure: from Recombination to Garching”, Banday, A. J. et al. (Eds.), astro-ph/9812350.
- Heideman, M.T., Johnson, D.H. & Burrus, C.S., 1984, “Gauss and the history of the FFT”, IEEE Acoustics, Speech and Signal Processing Magazine, Vol.1, 14.
- Janssen, M. et al., 1996, astro-ph/9602009.
- Kogut, A. et al., 1996, ApJ, 460, 1.

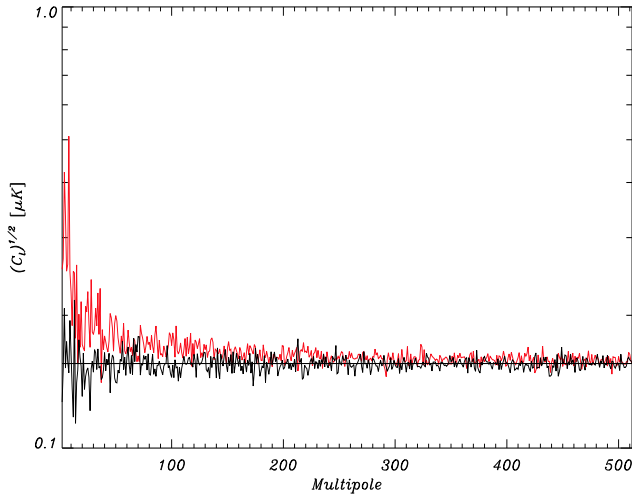


**Fig. 13.** Noise power spectra at 30GHz after destriping. Simulation parameters are the same of Fig. 12. The added noise is now only 2% of the white noise level. White noise spectra are also reported for comparison.

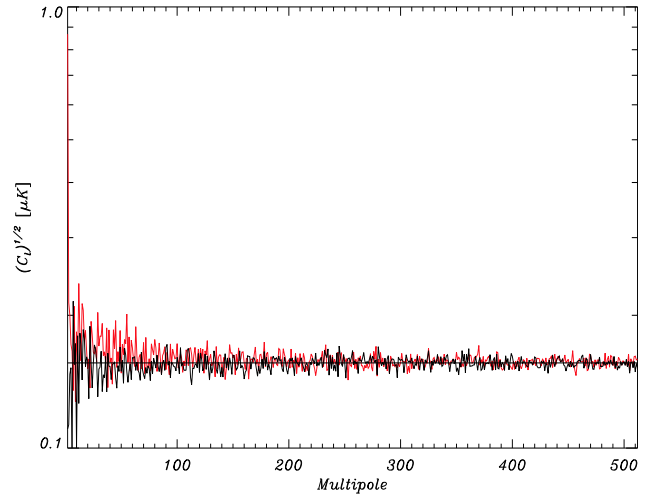


**Fig. 15.** Noise power spectra at 30GHz after destriping. Simulation parameters are the same of Fig. 14. The added noise is now only 0.5% larger the white noise level. White noise spectra are also reported for comparison.

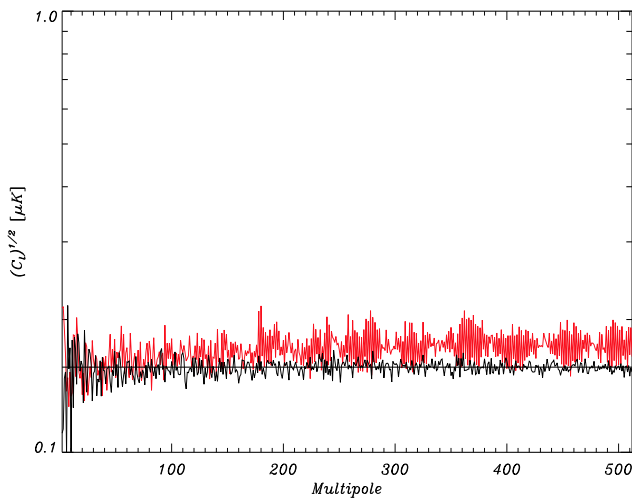


**Fig. 14.** Noise power spectra at 30GHz before destriping. Simulation parameters are the same of Fig. 4 but now  $f_k = 0.01$  Hz. The added noise is now only 9% of the white noise level. White noise spectra are also reported for comparison.

- Smoot, G.F. et al. , 1992, ApJ 396, L1.  
 Strang, G., 1976, “Linear Algebra and Its Applications”, Academic Press, Inc..  
 Wandelt, B. D. & Górski, K. M., 1999, in preparation.  
 Wandelt, B. D. et al. , 1999, Communication at the LFI Consortium Meeting, Firenze, 25-26 March 1999.  
 Wright, E. L., 1996, in IAS CMB Data Analysis Workshop, Princeton, 22 Nov 1996, astro-ph/9612006 .  
 Zaldarriaga, M. & Seljak, U., 1997, Phys. Rev. D., 55, 7368.

Lasenby, A. N., Jones, A. W., & Dabrowski, Y., 1998, Proceedings of the XXXIII<sup>rd</sup> Rencontres de Moriond, pg. 221.

Mandolesi, N. et al. , 1998, Planck LFI, A Proposal Submitted to the ESA.

Puget, J. L. et al. , 1998, HFI for the Planck Mission, A Proposal Submitted to the ESA.

Schlegel, D. J. et al. , 1998, ApJ, 500, 525.

Seiffert, M. et al. , 1997, Rev. Sci. Instrum, submitted.

This article was processed by the author using Springer-Verlag L<sup>A</sup>T<sub>E</sub>X A&A style file L-AA version 3.